

An Operational Method for Validating the Downward Shortwave Radiation Over Rugged Terrains

Guangjian Yan^{ID}, Senior Member, IEEE, Qing Chu^{ID}, Yiyi Tong^{ID}, Xihan Mu^{ID}, Jianbo Qi, Yingji Zhou, Yanan Liu, Tianxing Wang^{ID}, Donghui Xie^{ID}, Wuming Zhang, Kai Yan^{ID}, Shengbo Chen, and Hongmin Zhou^{ID}, Member, IEEE

Abstract—Estimation of downward shortwave radiation (DSR) is of great importance in global energy budget and climatic modeling. Although various algorithms have been proposed, effective validation methods are absent for rugged terrains due to the lack of rigorous methodology and reliable field measurements. We propose a two-step validation method for rugged terrains based on computer simulations. The first step is to perform point-to-point validation at local scale. Time-series measurements were applied to evaluate a three-dimensional (3-D) radiative transfer model. The second step is to validate the DSR at pixel-scale. A semiempirical model was built up to interpolate and upscale the DSR. Key terrain parameters were weighted by empirical coefficients retrieved from ground-based observations. The optimum number and locations of ground stations were designed by the 3-D radiative transfer model and Monte Carlo method. Four ground stations were selected to upscale the ground-based observations. Additional three ground stations were set up to validate the interpolated results. The upscaled DSR was finally applied to validate the satellite products provided by MODIS and Himawari-8. The results showed that the modeled and observed DSR exhibited good consistency at point scale with correlation coefficients exceeding 0.995. The average error was around 20 W/m² for the interpolated DSR and 10 W/m² for the upscaled DSR in theory. The accuracies of the satellite products were acceptable at most times, with correlation

coefficients exceeding 0.94. From an operational point of view, our method has an advantage of using small amount of ground stations to upscale DSR with relatively high accuracy over rugged terrains.

Index Terms—Downward shortwave radiation (DSR), field observations, rugged terrain, spatial interpolation and upscaling, validation.

I. INTRODUCTION

SURFACE downward shortwave radiation (DSR) is the radiative energy in the solar spectrum reaching the Earth's surface per time per unit area. It is the main driving force for the matter and energy cycle of the Earth system, playing a major role in the atmospheric and oceanic circulations, hydrological cycle, plant productivity, and climate change monitoring [1]–[4].

Land surface radiation monitoring mainly relies on ground stations and satellite observations [5]. Satellite radiation products are always validated by ground observations. Due to the importance of ground measurements, there are various observational networks established all over the world, such as the Global Energy Balance Archive (GEBA) [6], [7]; the Baseline Surface Radiation Network (BSRN) [8], [9]; the Surface Radiation Budget Network (SURFRAD) [10], [11] and the FLUXNET, which contains AsiaFlux, AmeriFlux, ChinaFlux, and so on [12]. However, rugged terrains cover approximately 24% of the Earth's land surface, playing an important role in the spatiotemporal distribution of DSR. With the demands of observations in mountainous areas, some related land surface experiments were implemented, such as the Global Energy and Water Cycle Experiment (GEWEX), Asian Monsoon Experiment on Tibetan Plateau (GAME/Tibet), and the Coordinated Enhanced Observing Period (CEOP) Asia–Australia Monsoon Project (CAMP). Some stations were also established in mountainous areas, such as nine stations from Alpine Surface Radiation Budget (ASRB) project in Switzerland [13], three stations in the Austrian Radiation monitoring network (ARAD) [14], two stations from the Watershed Allied Telemetry Experimental Research (WATER) program [15], [16], twelve stations in the north face of the Sierra Nevada Mountains in Spain [17], and five stations in the Guadalfeo river watershed in southern Spain

Manuscript received December 23, 2019; revised February 19, 2020; accepted April 28, 2020. Date of publication May 27, 2020; date of current version December 24, 2020. (Corresponding authors: Yiyi Tong; Xihan Mu.)

Guangjian Yan, Yiyi Tong, Xihan Mu, Jianbo Qi, Yingji Zhou, Yanan Liu, Donghui Xie, Wuming Zhang, and Hongmin Zhou are with the Faculty of Geographical Science, Beijing Normal University, Beijing 100875, China, also with the State Key Laboratory of Remote Sensing Science, Beijing Normal University, Beijing 100875, China, and also with the Institute of Remote Sensing and Digital Earth, Chinese Academy of Sciences, Beijing 100875, China (e-mail: tongyiyi0311@163.com; muxihan@bnu.edu.cn).

Qing Chu is with the Institute of Remote Sensing Science and Engineering, Faculty of Geographical Science, Beijing Normal University, Beijing 100875, China, and also with the Institute for Atmospheric and Climate Science, ETH Zurich, 8092 Zurich, Switzerland.

Tianxing Wang is with the State Key Laboratory of Remote Sensing Science, Beijing Normal University, Beijing 100875, China, and also with the Institute of Remote Sensing and Digital Earth, Chinese Academy of Sciences, Beijing 100875, China.

Kai Yan is with the School of Land Science and Techniques, China University of Geosciences, Beijing 100083, China.

Shengbo Chen is with the College of Geoexploration Science and Technology, Jilin University, Changchun 130061, China.

Color versions of one or more of the figures in this article are available online at <https://ieeexplore.ieee.org>.

Digital Object Identifier 10.1109/TGRS.2020.2994384

[18]. In mountainous areas, topographic effects are significant on steep slopes and in deep valleys. The slope gradients, aspects, and shadows could diversify surface radiation dramatically. However, the stations in these experiments were usually set up on relatively flat places. Besides, pyranometers were mostly leveled to provide measurements of radiation on a horizontal plane, which makes it difficult to validate the topographic effects with ground measured data [19], [20]. Only a few researches pay much attention to the slope-parallel observation in mountainous areas. Mayer positioned radiometers parallel to the slopes around Arizona's Meteor Crater to achieve the surface shortwave radiation for the validation of the MYSTIC model [21]. Wu *et al.* [22] compared the differences between observed irradiance and albedo between the horizontal and slope-parallel radiometers, proving that it is pivotal to have slope-parallel observations in the evaluation of satellite products. Wen *et al.* [23] concluded that when surface reflectance over rugged terrains is to be validated, whether the observation instrument should be parallel to the slope surface or the horizontal surface is a question that needs to be answered according to the definition of the study object.

A single measurement site is able to represent DSR over a large area on flat terrains, but this is not the case over rugged terrains [24], [25]. In mountainous areas, variabilities in elevation, surface orientation (slope and aspect), and shadows casted by surrounding terrains have a significant influence on the spatial distribution of DSR [26], [27]. The spatial variability limits the representativeness of the point-scale observations [28], [29]. Disparities of as much as 42% in the daily DSR are found between the exact energy received by a slope and the estimated values without consideration of topography [18].

As satellite products are developing from grid-level ($\geq 1^\circ$) to kilometer-level, we can no longer ignore the topographic effects on DSR retrieval. Usually, the validation of kilometer-level DSR is conducted by a direct comparison between the remote sensing products and ground-based measurements [30]–[33]. The mismatch of spatial scales is ignored and it is not clear whether the point-scale observations are representative of their surroundings or not. The error originating from their spatial sampling scales is defined as representativeness error [34]. A study revealed that even on flat terrains, 13% of errors are attributed to the inherent representativeness error for instantaneous products. Only when timescales are longer than or equal to one day, representativeness error can be ignored in validation [35]. But over rugged terrains, strong spatial heterogeneity will dramatically weaken the representativeness of point-scale observations and thus increase the validation error. Therefore, reasonable interpolation and upscaling method should be proposed to produce a reliable data set for satellite product validation. The widely used strategies can be categorized into three types. The most direct way is based on the statistical sampling theory including random, systematic, and stratified sampling [36]. A second strategy is to utilize the geostatistical-based algorithms, such as the block-Kriging, which predicts the spatial average while taking spatial autocorrelation into account [37]. A third strategy incorporates high-resolution remote sensing

images as auxiliary to bridge the spatial gap between point-scale observations and kilometer-scale products [38]. All these strategies have been applied to various study fields such as soil moisture [39], evapotranspiration [40], sensible heat fluxes [41], and LAI [42], [43]. But there are only a few studies paying special attention to solar radiation over rugged terrains. The DSR embodies distinctive characteristics different from other parameters. Its value over rugged terrains is dominated by the structure of land surfaces rather than the spectrum of land covers. The terrain factors and atmospheric conditions act as controlling factors to the spatial distribution of the energy. The high heterogeneity of DSR and the difficulty in field campaign make the validation not a trivial work, implying the great necessity to challenge the DSR validation aporias over kilometer-scale rugged terrains.

In this framework, we propose a methodology to validate DSR in mountainous areas. The ground observations at various locations provided truth values at point-scale. The simulation of a three-dimensional (3-D) radiative transfer model and Monte Carlo method were used to locate the ideal ground stations. A semi-empirical model was developed to upscale the point-scale DSR to kilometer-scale. This article is organized as follows: In Section II, the data sets, procedures of field experiments, and the principle of interpolation and upscaling method are elucidated. In Section III, the performances of point-scale DSR validation, interpolation, and upscaling results are evaluated. Discussions about cloud effects on the results and comparison with traditional upscaling method are presented in Section IV. Finally, Section V summarizes the main points of this article.

II. DATA AND METHODS

A. Study Area and Data

1) *Study Area*: The study area locates on the Moon Mountain of Saihanba Forest Park ($42^\circ 23'N$, $117^\circ 24'E$) in Chengde, northeast of China. Two regions of interest were chosen to cover an area of $5 \text{ km} \times 5 \text{ km}$ and $2 \text{ km} \times 2 \text{ km}$, respectively [Fig. 1(a)]. The large region served as the pixel-scale validation district corresponding to the spatial resolution of satellite products. The subregion functioned as the point-scale validation district and the experimental field for DSR interpolation and upscaling, considering the accessibility of the mountains and the operability of our experiments. It was dominated by rugged terrains with the elevation ranging from 1660 to 1890 m. The digital elevation model (DEM) data generated by Ziyuan III satellite (ZY3) with a resolution of 12.5 m were utilized in our study [Fig. 1(b)] for elaborate calculation of terrain parameters. The land surfaces are mainly covered by grasses, with a certain amount of shrubs and trees patching over the region in spring and summer [Fig. 1(c)], making it feasible for the installation and maintenance of ground stations.

2) *Data Sets*: Over the $2 \text{ km} \times 2 \text{ km}$ study area, we conducted two experiments to obtain point-specific measurements. In the first experiment, the DSR data were collected from July to August in 2015, while the ground stations in the second experiment have been on operation since August 10, 2018.

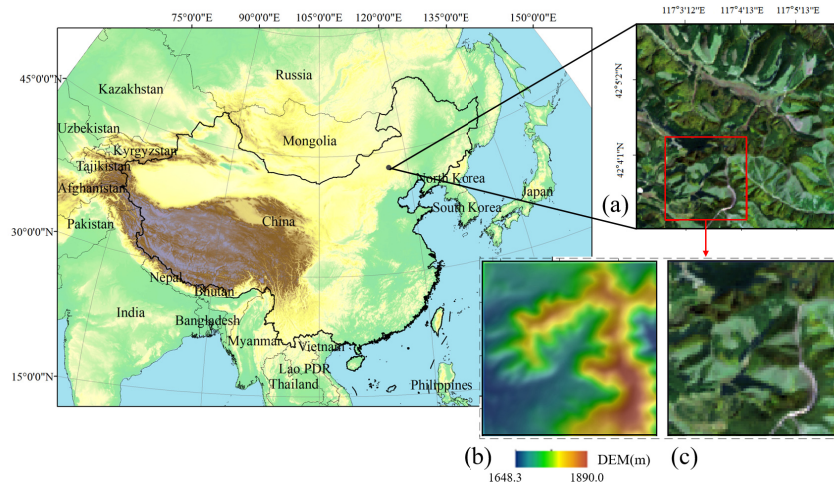


Fig. 1. Topographic characteristics of the study area, including (a) locations of the $5 \text{ km} \times 5 \text{ km}$ and $2 \text{ km} \times 2 \text{ km}$ study areas, (b) DEM data, and (c) Landsat8-OLI image of the subregion.

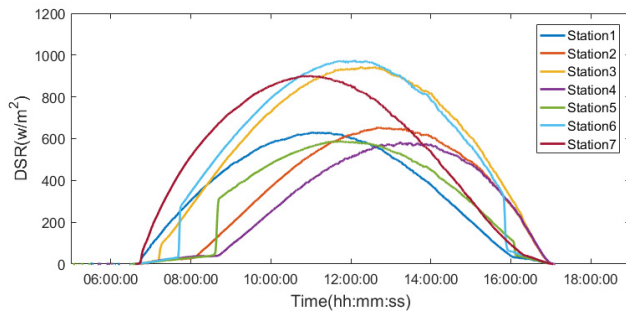


Fig. 2. Measured DSR at different slopes on November 2, 2018.

Fig. 2 gives an example of the observed data. Detailed information about the ground stations and data sets can be seen from the Appendix. Different slopes, aspects, and surrounding terrains make the temporal variation of DSR varied significantly. Over rugged terrains, the amplitude and phase positions of diurnal radiation curves change with the local sun-terrain geometry. The sunlit duration time of a station is determined not only by the solar position but also by the shadows caused by topography. It proves that spatial heterogeneity of DSR is dramatically strengthened under topographic effects [44].

Over the $5 \text{ km} \times 5 \text{ km}$ study area, we chose two types of kilometer-scale DSR products to be validated on account of the accessibility and continuity of the satellite data. The first product is the L3 shortwave radiation data derived from the Himawari-8 satellite, which provides DSR at 1-h scale with a resolution of 5 km (available at <ftp://ftp.ptree.jaxa.jp>). The shortwave radiation parameterization method is based on the work of Frouin and Murakami [45]. The second product is the gridded 5-km DSR generated from MODIS data (MCD18A1), which supplies instantaneous DSR at the satellite overpass time and interpolated estimates at 3-h intervals (available at <https://ladsweb.modaps.eosdis.nasa.gov/search/>). The basic framework was presented by Liang *et al.* [46] for estimating photosynthetically active radiation (PAR). The time-series data

of the two products were extracted from October 30, 2018 to November 30, 2018.

B. Point-Scale Validation Method of DSR

The bottleneck for the validation of satellite products is the mismatch of spatial scales. Over rugged terrains, the validation methodology of DSR can be decomposed into two steps referring to the conventional level-by-level or hierarchical validation approach. The first step is to perform point-to-point validation at local scale. Point-specific observations are obtained to evaluate the high-resolution DSR simulated by physical models. The second step is to yield upscaled predictions for the validation of satellite products. The scale gap will be filled with an effective interpolation and upscaling method, which will be discussed in Section II-C.

In the first step, the acquirement of reliable point-scale observations is the prerequisite for a holistic validation system. Considering the complicated characteristics of rugged terrains, the ground stations were set up on varied terrains to ensure the representativeness of spatial samplings. The two observational methods measure different downward radiation on slopes, as illustrated in Fig. 3. The parallel slope method in Fig. 3(b) and (c) measures the direct, diffuse, and terrain-reflected irradiance from the hemisphere Ω_1 , which is consistent with the three components of DSR reaching to slope surfaces. While as shown in Fig. 3(d) and (e), the radiometer is set up at a horizontal level, which contradicts with the underlying inclined surface. In this way, the radiation coming from Ω_2 will be measured instead of Ω_1 . Moreover, the illumination angle of local slope is consistent with the angle between the direct beam and the normal of the radiometer plane in Fig. 3(c), which largely determines the measured direct irradiance. In our study, we adopted the first observational method. The radiometers were mounted parallel to the land surfaces [Fig. 3(a)] on a portable tripod ranging from 1.5 to 3 m above the ground.

A Large-Scale remote sensing data and image Simulation framework (LESS) is capable of depicting the

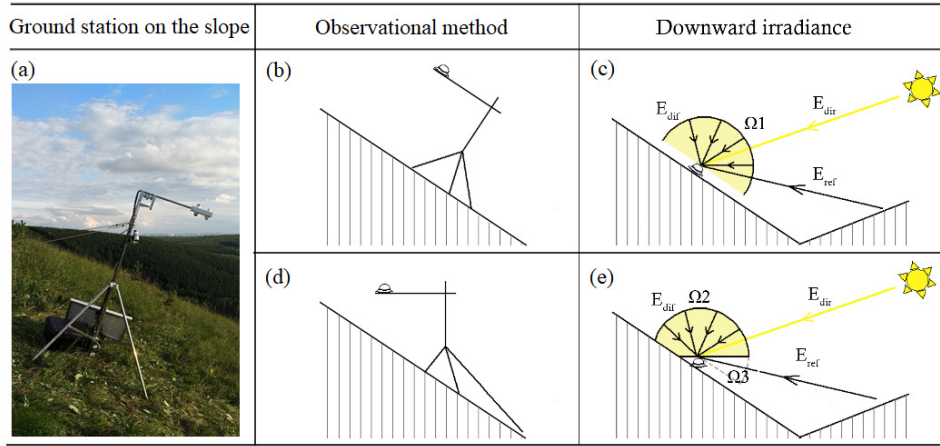


Fig. 3. Installation of ground stations and the two observational methods for DSR on slope surfaces. E_{dir} , E_{dif} , E_{ref} are the direct irradiance, diffuse irradiance, and terrain-reflected irradiance the slope received, respectively.

complicated radiative transfer process in the context of real scenes [47], [48]. It employs a forward photon tracing method to simulate flux data and has an advantage over other 3-D radiative transfer models in computation efficiency. LESS has been compared with other models from the RAdiative transfer Model Intercomparison (RAMI) experiment and validated with field measurements in the previous study, guaranteeing the accuracy of radiative simulation. More information about the LESS model is on the website (<http://lessrt.org>).

We chose LESS as a tool for DSR upscaling. First, it was validated at point-scale. With high-resolution DEM data as the input, three components of DSR were simulated separately. By setting the surface albedo as zero, we simulated direct and diffuse irradiance over rugged terrains with only direct and only diffuse irradiance over flat terrains as inputs, respectively. The terrain reflected irradiance was the rest part of the total irradiance subtracted by the sum of direct and diffuse irradiance over rugged terrains. The spatial resolution of the simulated DSR is consistent with the input DEM data (12.5 m). The *in situ* observed DSR can match with the spatial scale of simulations, as we carefully selected the slopes to be uniform within the simulated pixels and thus the spatial heterogeneity can be ignored. Fig. 4 gives an example of the simulation results over the study area. In terms of qualitative analysis, direct irradiance is in tight relation to slope orientations and solar directions, thus showing higher values on east-facing slopes than west-facing slopes in the morning. Diffuse irradiance is dominated by the scattered sunlight coming from the visible upper-hemisphere. It approaches the maximum value at hilltops and open areas, while comparatively low values at valleys and slopes due to the obstruction of surrounding terrains. By contrast, the terrain-reflected irradiance contradicts with diffuse irradiance by showing higher values in valleys as adjacent mountains can make a great contribution to multi-scattering energy. In terms of quantitative evaluation, modeled and observed DSR were compared at various times and places. To mimic the real environmental conditions, we used the measured direct and diffuse irradiance on the flat hilltop as

inputs for the LESS model on cloud-free days. Combined with the solar geometry and the measured surface albedo, the point-scale DSR at ground stations was calculated by LESS and then validated by the measurements on the slopes. To control the geometric registration between them, we measured the local geographic coordinates, slopes, and aspects with the global positioning system (GPS) and the compass. Thus, we can find the exact locations of the ground stations from the DEM and extract the *in situ* DSR from the LESS simulations to match with the ground observations.

Apart from the field validation, we performed the inter-comparison between the LESS and the traditional Mountain Radiative Transfer model, which we called MRT in this article. In the MRT model, the direct irradiance can be expressed by the product of the vertical incidence on horizontal surfaces ($I_{dir,\perp}^{\downarrow}$) and the cosine angle between the incident ray and the slope surface normal (cosis), which is expressed as

$$\text{cosis} = \cos(\text{SZA}) \cos(S) + \sin(\text{SZA}) \sin(S) \cos(\text{SAA} - A) \quad (1)$$

where SZA and SAA denote solar zenith angle and solar azimuth angle; S and A denote slope and aspect. Moreover, some slopes may be sheltered and unable to receive direct radiation from the sun. A Boolean shadow factor Θ is introduced to reflect whether the target slope is sunlit or not [49], [50]. Therefore, the direct irradiance can be calculated as

$$I_{dir}^{\downarrow}(\text{SZA}, \text{SAA}, \text{DEM}) = \Theta \times I_{dir,\perp}^{\downarrow} \times \text{cosis}. \quad (2)$$

The diffuse irradiance is the product of the sky irradiance on a flat surface (I_{dif}^{\downarrow}) and the sky view factor (Vd) which represents the portion of the overlying hemisphere visible to a pixel [51]. This radiation component is expressed as

$$I_{dif}^{\downarrow}(\text{DEM}) = I_{dif}^{\downarrow} \times Vd(\text{DEM}). \quad (3)$$

The adjacent-terrain reflected radiation is obtained through the method established by Proy *et al.* A computation-demanding iterative process is required to take into account the multi-scattering. Finally, the DSR over rugged terrains is the

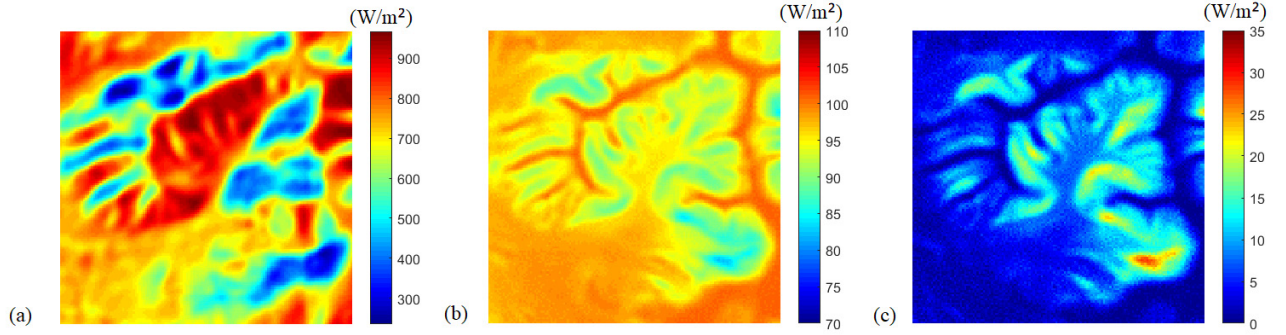


Fig. 4. Three components of DSR simulated by LESS at 10:00 A.M. on August 15, 2015. (a) Direct irradiance. (b) Diffuse irradiance. (c) Terrain-reflected irradiance.

sum of the three components with the measured direct and diffuse irradiance on the flat hilltop as inputs. To avoid the uncertainties in calculating direct and diffuse irradiance over flat terrains, the $I_{dir,\perp}^{\downarrow}$ and I_{dif}^{\downarrow} in the above equations were represented by the ground observations on the flat hilltop. Detailed illustrations about the shadow factor and the sky view factor are provided in the Appendix. In a nutshell, the MRT model serves as a useful auxiliary to evaluate the LESS model and to illustrate our semi-empirical algorithm in Section II-C.

To perform the quantitative validation, the Pearson correlation coefficient (R^2), the root mean squared error (RMSE), the discrete Fréchet distance (DFD) [52], [53], and the mean error (ME) were applied to assess the validation results, which are expressed as follows:

$$R^2 = \frac{\sum_{i=1}^n (M_i - \bar{M})(O_i - \bar{O})}{\left[\sum_{i=1}^n (M_i - \bar{M})^2 \sum_{i=1}^n (O_i - \bar{O})^2 \right]^{1/2}} \quad (4)$$

$$RMSE = \sqrt{\frac{\sum_{i=1}^n (M_i - O_i)^2}{n}} \quad (5)$$

$$DFD = \min\{\max[d(M_{ai}, O_{bi})]\} \quad (6)$$

$$ME = \left(\sum_{i=1}^n M_i - \sum_{i=1}^n O_i \right) / n \quad (7)$$

where n is the number of data over a day; M_i and \bar{M} are the modeled instantaneous DSR and daily average DSR; O_i and \bar{O} are the observed instantaneous DSR and daily average DSR; M_{ai} and O_{bi} are the samplings of the modeled and observed diurnal DSR curves. The operator d indicates the Euclidean distance of the two sampling points. The R^2 and RMSE measure the discrepancy between the modeled and observed instantaneous DSR. The discrete Fréchet distance measures the resemblance of diurnal variation and the mean error evaluates the accuracy of daily mean DSR.

C. Interpolation and Upscaling Method of DSR

Disparity in spatial scales between ground-based observations and satellite products highlights the significance of

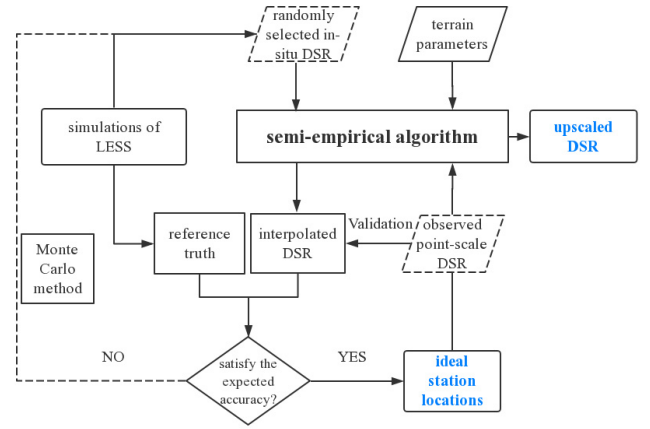


Fig. 5. Flowchart of the interpolated and upscaling scheme.

interpolating and upscaling point-scale observations for pixel-scale validation. Large-scale differences pose serious challenges of the procedure, which arise from not only the strong heterogeneity caused by rugged terrains, but also the sparsely located nodes which are insufficient to capture the spatial variation of DSR. Thus conventional upscaling methods fail to achieve acceptable accuracy with densely observing network hardly practical on mountains. Therefore, we spearhead major efforts to propose a method for DSR interpolation and upscaling over rugged terrains. The whole scheme is illustrated in Fig. 5. First, we developed the semi-empirical algorithm for interpolation and upscaling. Second, the simulations of LESS were treated as the reference truths to help locate the ideal ground stations through Monte Carlo method. Third, the semiempirical algorithm combined with the geo-statistical method was applied to upscale the *in situ* observations.

To be specific, the spatial distribution of DSR over rugged terrains is highly correlated with the topography, which has been quantitatively interpreted in the MRT model. Considering its wide applications, we introduce several key terrain parameters from the model to our interpolation method; including the Boolean shadow factor Θ , the cosine angle between the incident ray and the slope surface normal $\cos\theta$ and the sky view factor V_d . These parameters can be determined in advance given the DEM and the solar position. However,

it is hard to obtain the irradiance components on flat surfaces over rugged terrains and thus we have to treat the irradiance on the flat hilltop as inputs for the MRT model (Section II-B). But to interpolate and upscale the point-scale DSR, the observations at the limited flat surfaces cannot represent the whole conditions over a pixel-scale region. To make use of more observations on the widely-distributed slope surfaces, we developed the semi-empirical interpolation algorithm as follows:

$$\text{DSR}^{\text{interpolated}} = C_1 \times \Theta \times \text{cosis} + C_2 \times Vd + C_3. \quad (8)$$

The algorithm has a similar form with the MRT model to partially retain the physical principle. It indicates that the interpolated DSR is the sum of *in situ* terrain parameters weighted by three coefficients (C_{1-3}) assuming to be constant over a pixel. The coefficients can be interpreted as the inputs for the MRT model but their values can be quite different from the observed irradiance on the flat hilltop. At least three equations are required to retrieve them, which means that more than three ground-based observations are demanded on different slopes. Through this way, more information over rugged terrains can be incorporated into DSR interpolation. A global optimal method, Shuffled Complex Evolution (SCE-UA) [54], was applied to obtain the optimal coefficients at different times. All the coefficients were set beyond zero to represent positive contributions of the three components to the interpolated DSR.

Given the limited number of equipment and the spatial variation of atmospheric and topographic conditions, the locations of ground stations should be carefully selected to make the coefficients capable of representing the average irradiance reaching to each slope. Ideal station locations can be decided by the Monte Carlo method and the LESS model. In this framework, DSR simulated by LESS was used as the reference truth. The Monte Carlo method was applied to carry out the random selections of ground stations at accessible locations. First, regions occupied by trees and steep slopes were removed from the possible locations with the help of the pseudo-color image provided by Landsat8-OLI, true-color image supplied by Google Earth, and the slope gradients retrieved from DEM. Detailed procedures are explained in Section II-B. Second, we randomly scattered a given number of points, which equals the number of stations, over the accessible locations at one time. Third, at the randomly selected locations, point-scale DSR values were extracted from the simulated DSR to mimic the ground-based observations. Considering the representativeness of point-scale observations, simulations were performed under different atmospheric conditions involving varied visibility, relative humidity, and ozone thickness over a long period. And then we applied the semi-empirical model to interpolate the point-scale DSR. The interpolated results were compared with the reference truths provided by the LESS simulations. The discrepancy between them was recorded. Finally, steps 2 and 3 were repeated millions of times until the expected accuracy was achieved or the iteration number reached the predetermined threshold. During the procedure, the selected locations with the least discrepancy were treated as the optimal

stations. Besides, additional ground stations were set up on diversified slopes for the validation of interpolated DSR.

We assume that the pixel-scale $\text{DSR}^{\text{region}}$ can be decomposed to a deterministic spatial pattern $\text{DSR}^{\text{pattern}}$ and a stochastic residual R , given by

$$\text{DSR}^{\text{region}} = \text{DSR}^{\text{pattern}} + \bar{R} \quad (9)$$

where $\text{DSR}^{\text{pattern}}$ is the spatial average of the interpolated DSR over a region. It represents the component of pixel-scale DSR dominated by the deterministic topography configurations. And \bar{R} reflects the average discrepancies between the interpolated and the real DSR at each slope, which is determined by the stochastic atmospheric conditions. In practice, the real DSR given by ground observations is not accessible everywhere. The Ordinary Kriging method [55] was applied to interpolate the residuals with the limited ground stations. It is reasonable to assume that the residual component is spatially correlated, typically indicating the small-scale, “noisy” variation mainly resulting from cloud effects. Based on the hypothesis of second-order stationary, the interpolated residual can be estimated through the semi-variogram which is expressed as [56]

$$\gamma(h) = \frac{1}{2n} \sum_{i=1}^n [R(x_i) - R(x_i + h)]^2 \quad (10)$$

where $R(x_i)$ represents the residual at location x_i and h is the distance between the two stations. Multiple fitting functions including the spherical, exponential, and Gaussian algorithms have been proposed to derive a continuous variogram, which is characterized by three parameters: nugget, sill, and range. Once the theoretical variogram is obtained, the residuals can be interpolated to predict \bar{R} , which is the average of all the $R(x_i)$. The final $\text{DSR}^{\text{region}}$ is the sum of $\text{DSR}^{\text{pattern}}$ and \bar{R} , and can be treated as an unbiased and optimal estimation of pixel-scale DSR.

D. Pixel-Scale Validation Method of DSR

The upscaled DSR serves as the reference truth to directly validate the satellite products retrieved from Himawari-8 and MODIS. The products were marked as clear or cloudy by the meteorological measurements using all-sky cameras. We avoided the use of cloud-screening products to diminish the uncertainties of satellite data. When compared against the Himawari-8 products, the upscaled DSR was averaged within a 10-minute time window around the time from 8:00 to 18:00 with 1-h interval every day. When validating the MODIS DSR, the time window was set as 30 minutes around the MODIS 3-h product time. The validation was performed from October 30 to November 30, 2018. The index used to assess the validation results were similar to those applied in Section III-B, which include R^2 , RMSE, and ME.

III. RESULTS AND ANALYSIS

In this section, we will give a detailed analysis about the point-scale validation results, the performances of ground observations, the corresponding interpolation and upscaling results, and the pixel-scale validation assessments.

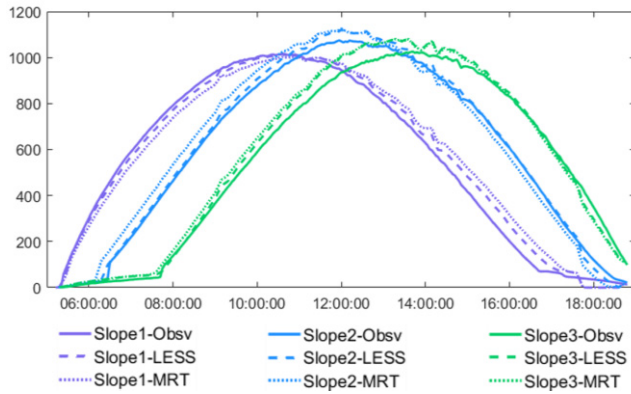


Fig. 6. Comparison between the DSR simulated by LESS, MRT, and ground observations on August 15, 2015. Slopes 1, 2, and 3 indicate east-facing, south-facing, and west-facing slopes, respectively.

First, the point-scale DSR extracted from the LESS simulation is validated using ground-based observations. Second, the process of locating ground stations for upscaling is demonstrated. Third, the point-scale DSR is interpolated and validated by additional ground-based measurements. Finally, a reliable pixel-scale DSR data set is yielded and applied to validate the MODIS and Himawari-8 DSR products.

A. Evaluation of the LESS Model

As the LESS and MRT models are unable to consider the cloud effects on DSR, we only give an example of the validation results on a cloud-free day. As shown in Fig. 6, the DSR simulated by LESS is in good consistency with the observations on slopes and the MRT model. Compared with the ground observations, slight overestimation occurs on the east-facing slope in the afternoon. On the west-facing slope, there are obvious differences in the morning, especially at the midday. The best match takes place on the south-facing slope with only a short period of deviations around the midday. Compared with the MRT model, the results show greater consistency on the three slopes. On the east-facing and the south-facing slopes, the DSR simulated by MRT is more deviated from the ground observations than that simulated by LESS. On the west-facing slope, the two models are highly correlated.

Quantitative analysis with ground observations is provided in Table I. The simulations on three slopes all show a strong correlation to the observations with R^2 above 0.995. But the RMSE values on two slopes both exceed 30 W/m^2 except that on the south-facing slope. Several possible reasons are responsible for the considerable discrepancy. One explanation is that the terrain reflected irradiance is susceptible to the surface albedo, which is set as a constant value of 0.2 based on sampled observations, failing to reflect the real spatial and temporal variation of the surface reflectance. Another reason is that the inclination and orientation angles of radiometers differ from the slopes and aspects derived from DEM. It can be attributed to the imprudence in locating the instrument planes or the misrepresentation of the true local topography

TABLE I
QUANTITATIVE VALIDATION OF THE DSR SIMULATED BY LESS

	Slope1	Slope2	Slope3
R^2	0.996	0.999	0.996
RMSE (W/m^2)	35.784	23.967	44.424
DFD	31.104	49.889	55.026
ME (W/m^2)	11.700	13.552	25.682

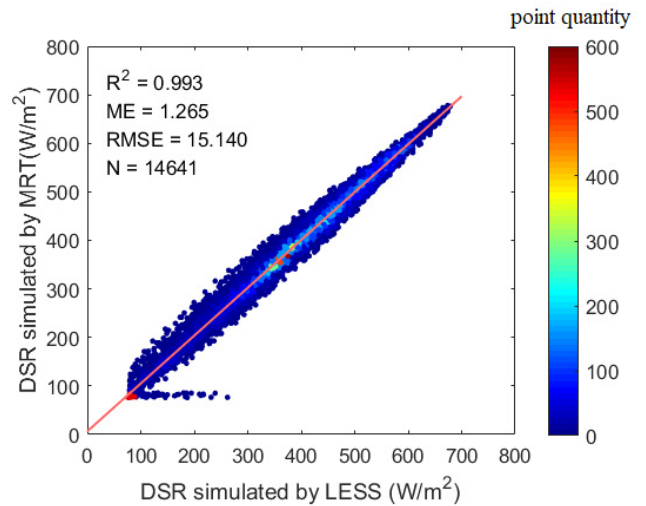


Fig. 7. Intercomparison between the LESS and MRT models at various times and places. The color scale represents the point quantity.

by crude DEM. By contrast, the DFD index indicates that the best similarity between the modeled and observed diurnal curves occurs on the east-facing slope. Concentrating on the trend or prediction of DSR over a time period, DFD acts as a favorable index to evaluate the modeled results. Despite the discrepancies in instantaneous DSR validation, the ME on three slopes is all less than 30 W/m^2 . As a result of the lack of sufficient observation data for comprehensive evaluation, we further implement the cross-validation between the LESS and MRT models at various times and places. As shown in Fig. 7, the two models are in great consistency with R^2 higher than 0.99 on various slopes and RMSE around 15 W/m^2 . However, large discrepancies occur on the left bottom with the MRT simulations fixed at around 80 W/m^2 while the LESS simulations ranging from 80 to around 280 W/m^2 . The reason is that the LESS model is able to consider the half-shadowing within a pixel, while the MRT model treats a pixel as sheltered or not-sheltered. Therefore, at around sunrise and sunset, the MRT model will underestimate the DSR at some pixels. The result proves that the LESS model is more reliable and satisfies our needs for providing a priori information to the following study.

B. Allocation of the Ground Stations

Based on the verified LESS model and the proposed interpolation and upscaling method, we used the Monte Carlo method to decide the optimum number and locations of ground

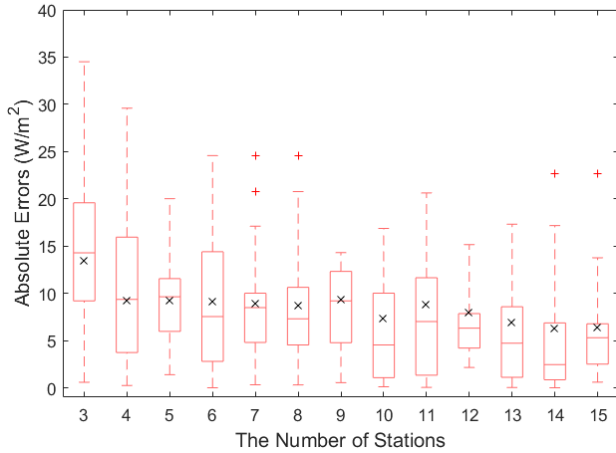


Fig. 8. Upscaling errors change with the number of ground stations. The box plot in red is used to depict the statistical characteristics of upscaling errors. The five horizontal lines from upper to lower indicate maximum, 75th percentile, median, 25th percentile, and minimum values. The red plus markers represent outliers while the black cross markers indicate the mean values of absolute errors over a cloud-free day.

stations. Fig. 8 gives an example of the upscaling errors over a cloud-free day. Absolute errors show the discrepancies between the upscaling results and the pixel-scale DSR derived from the LESS model. The box plots reflect the temporal distributions of instantaneous errors over a day. The average errors are not more than 15 W/m^2 for the instantaneous DSR. With the increase of ground stations, large errors can be slightly suppressed but not avoided due to the uncertainties embedded in the Monte Carlo simulation. The settings of the expected accuracy (20 W/m^2) and the number of iterations (1 million) were tentative at this procedure. Regardless of the random errors, Fig. 8 highlights the prominent advantage of the proposed method, which can curb the overreliance on ground-sampling density in DSR upscaling. It is evident that four ground stations are sufficient to achieve the acceptable accuracy level with the average error below 10 W/m^2 for upscaled DSR in theory.

After clarifying the upscaling method's sensitivity to the number of ground stations, three factors were taken into account in allocating the ground stations. First, in light of the distance between trees and radiometers demanding ten times larger than their elevation difference, the regions dominated and effected by trees were regarded as prohibited locations for ground stations. Second, steep slopes with gradients larger than 35° were abandoned considering the difficulty of setting up instruments [Fig. 9(a)]. Third, hardly can we manage to retrieve the coefficients in (8) with any variable equal to zero at all ground stations. The most likely condition is that all the slopes we choose are shaded in the morning or evening, making it impossible to estimate C_1 and DSR on sunlit slopes. Therefore, the regions without shadowing at sunrise and sunset are required [Fig. 9(b)]. The intersection regions of the satisfactory and required locations are demonstrated in Fig. 9(c). In view of all the constraints, the expected accuracy was set with RMSE below 45 W/m^2 according to

the validation results at point-scale. And the iteration number is set as 10 million for the Monte Carlo method to avoid the aforementioned uncertainties. The ideal locations for ground stations were determined with the least differences between the interpolated and modeled DSR under variant atmospheric conditions at different times. Given the field conditions and experiment resources, four radiometers were finally set up at the optimized locations (Stations 1–4) for interpolation and upscaling. Three additional stations (Stations 5–7) were installed at the possible locations [Fig. 9(a)] for validation of the interpolated DSR as shown in Fig. 9(d). Detailed information of the seven ground stations is exhibited in the Appendix.

C. Performances of the Interpolation and Upscaling Method

As illustrated in Section II-C, the coefficients are retrieved through the observed DSR at four ground stations [Stations 1–4 in Fig. 9(c)]. On a cloud-free day (November 13, 2018), daily variation of the three coefficients is demonstrated in Fig. 10(a). The curve of C_1 resembles the sinusoidal line of DSR on flat surfaces, indicating the diurnal cycle of DSR dominated by the solar position. The curves of C_2 and C_3 exhibit slightly random fluctuations over a day arising from the variation of atmospheric conditions. Based on the coefficients and the pre-calculated terrain parameters, the DSR pattern is demonstrated in Fig. 10(b). To illustrate the topographic effects on DSR, the observations at the flat hilltop are presented as comparison. Although both of them show similar trend over a day, obvious discrepancies are barely smoothed at a kilometer-scale pixel. The undulated topography prevents a small portion of DSR reaching to the surfaces before noon, but a slight compensation is rendered in the afternoon. Such a phenomenon can be explained by the topographic characteristics over the $2 \text{ km} \times 2 \text{ km}$ study area, where the west-facing slopes are more clustered than the others. Moreover, the spatial heterogeneity is strongly enhanced as depicted by the gray shadow region and the coefficient of variance (C_v) in Fig. 10(b). At noon, the standard deviation reaches the peak due to the large value of DSR. We use C_v , which is the standard deviation divided by the mean value, to further demonstrate the daily variation of the spatial heterogeneity. As the time gets closer to the noon, the SZA decreases and makes energies more uniformly distributed in the area due to fewer places obscured by mountains. More detailed analysis can be found in our previous research [44]. The result highlights the necessity to accommodate topographic effects into DSR interpolation and upscaling.

Furthermore, the residuals at each station were calculated and then applied to the Ordinary Kriging method to obtain the \bar{R} in (9). The accuracy of \bar{R} is not guaranteed with sparsely located ground stations. However, the spatial variation of atmospheric conditions is not significant on cloud-free days. The residuals at different slopes are relatively small and consistent, making it reasonable to overlook the uncertainties caused by insufficient samplings. It is advantageous to evaluate our method on cloud-free days. As demonstrated in Fig. 11, the pixel-scale DSR is composed of the \bar{R} and DSR pattern,

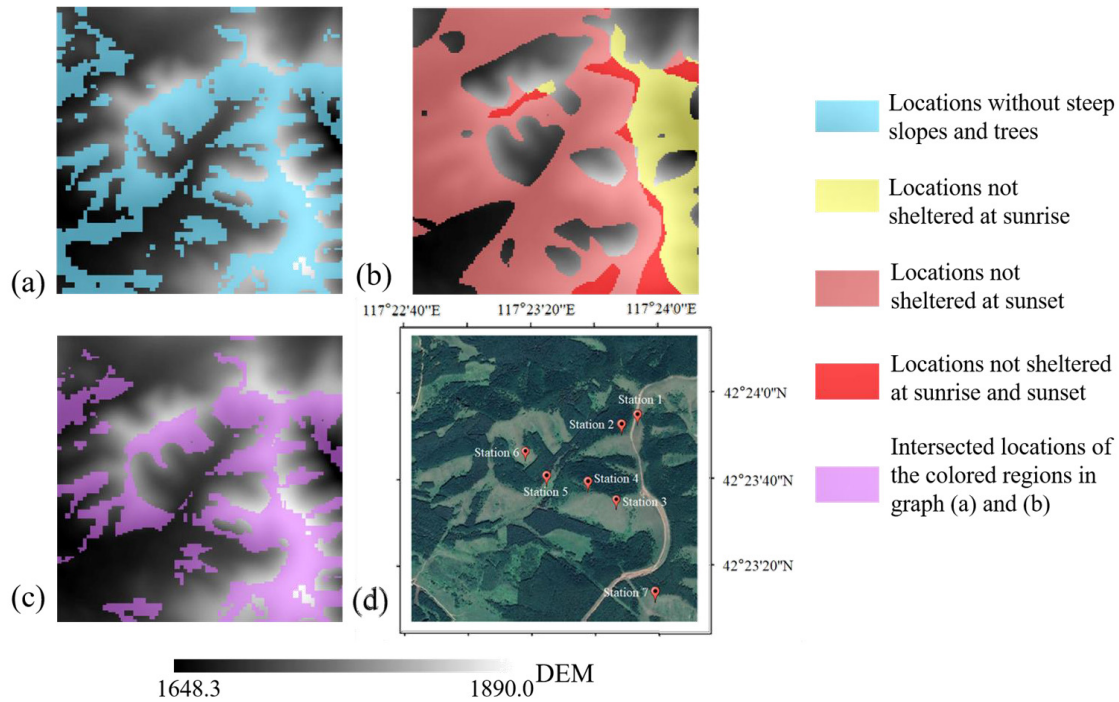


Fig. 9. Process of locating ground stations. (a) Possible locations (in blue) after removing steep slopes and trees. (b) Required locations without shadowing at sunrise (in yellow) and sunset (in light red), respectively, and the intersection region (in deep red). (c) Intersected locations of the possible locations and the required locations. (d) Final locations of ground stations.

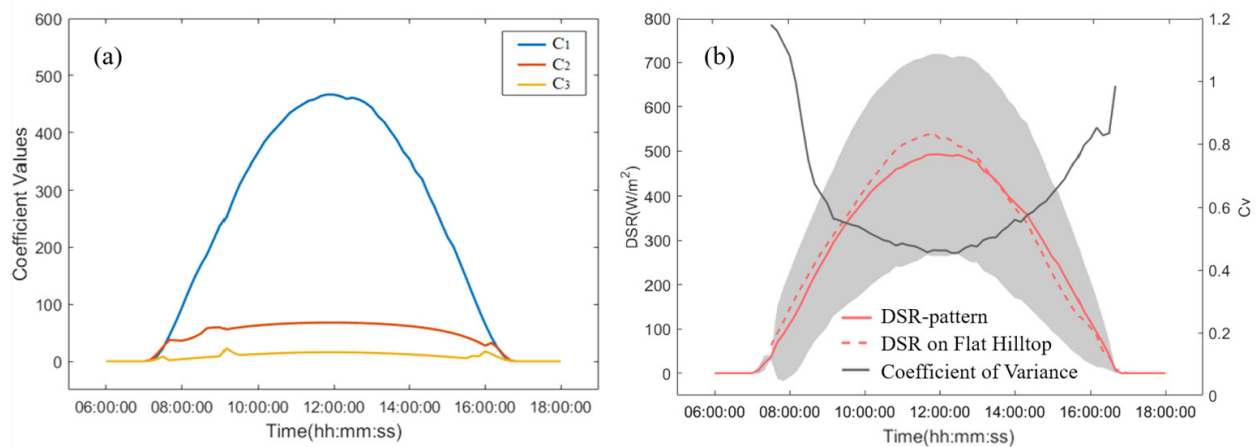


Fig. 10. Retrieved coefficients and DSR pattern over a cloud-free day. (a) Variation of coefficients over a day. (b) Comparison between the DSR pattern and the measured DSR on a flat hilltop corresponding to the left vertical axis. The gray shadow region indicates the spatial variation of the interpolated DSR with one standard deviation around averages. The coefficient of variance (Cv) indicates the spatial heterogeneity of DSR (corresponding to the right vertical axis).

which plays a dominant role in the upscaled result. Regardless of minor contributions at most times, the residuals partially compensate for the errors around sunrise and sunset, when the abrupt change of radiation is hard to be captured.

D. Validation of the Interpolated DSR

Due to a lack of reliable pixel-scale DSR data sets, validation of the interpolated DSR serves as an indirect approach to evaluate the proposed upscaling method. It is achieved by additional observations at Stations 5–7 [Fig. 9(c)] as a

comparison with the interpolated values. As demonstrated in Fig. 12(a), the observed and estimated DSR show favorable consistency at Stations 1–4 with R^2 beyond 0.99 and RMSE below 25 W/m^2 over the cloud-free days during a month. Although a small number of points deviate from the diagonal line, the overall result proves that the retrieved coefficients are applicable at pixel-scale. As demonstrated in Fig. 12(b), the errors climb slightly at Stations 5–7 with R^2 beyond 0.985 and RMSE below 45 W/m^2 . Obvious deviations mainly expose at the left bottom of the diagonal line with relatively small values of DSR. Such a phenomenon again reveals that

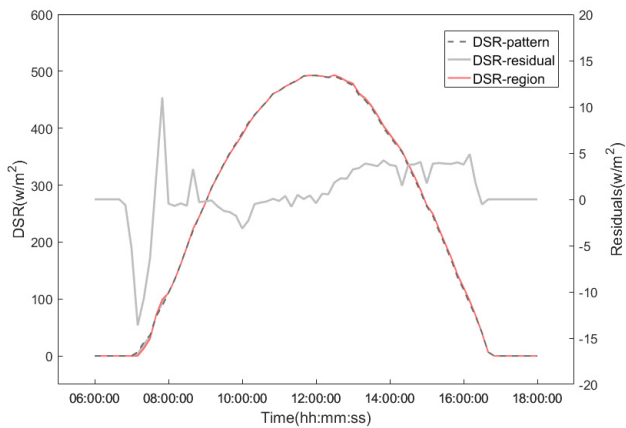


Fig. 11. DSR pattern, pixel-scale DSR (corresponding to the left vertical axis), and the residuals (corresponding to the right vertical axis) over the $2 \text{ km} \times 2 \text{ km}$ study area on a cloud-free day.

great uncertainties are inevitable around sunrise and sunset time. Another small magnitude of bias along the diagonal line possibly stems from the local disturbance by clouds or embedded errors in the coefficients, which are unlikely to be subtle appropriate for all the slopes. As the errors of point-scale validation can reach 44 W/m^2 due to uncertainties in topographic parameters and *in situ* observations (Table I), the interpolated error is acceptable and our method is applicable to pixel scale. Furthermore, the residual \bar{R} can be used to decrease these interpolation errors in DSR upscaling.

To give a whole picture of the upscaling results, the $2 \text{ km} \times 2 \text{ km}$ DSR on cloud-free days is depicted in the temporal domain as shown in Fig. 13. From October 30 to November 30, 2018, the total radiation reaching to the surfaces has experienced a steady decrease, while the diurnal variation of DSR was similar on each day. Small fluctuations occurred on occasion as a result of the disturbance by clouds or abrupt change of atmospheric conditions. At most time, the interpolated errors are less than 20 W/m^2 for instantaneous DSR. But the discrepancies become significant around sunrise and sunset without exception, which is consistent with the result in Fig. 12. It indicates that the problems embedded in the calculation of interpolated DSR rather than the uncertain external factors. The inaccuracy of terrain parameters, especially the shadow factor, is to be blamed for considerable errors. On one hand, it is hard to capture the abrupt change of shadows without pinpoint DEM data. On the other hand, the uncertainties are irradicable in locating the radiometers planes. Therefore, the errors propagate from the terrain parameters to the coefficients and the interpolated DSR through (8). The histogram in Fig. 13 indicates that the errors are not more than 30 W/m^2 at most times and the average error is 20 W/m^2 . At around 4% of the total time, the errors exceed 60 W/m^2 , which are acceptable for instantaneous DSR estimation. As the temporal scale changing from instantaneous to hourly and daily and the spatial resolution varying from point-scale to pixel-scale, the interpolated errors will be significantly suppressed [35], [57]. In light of this, the upscaled DSR has the potential to become an accuracy-accepted data set for the validation of satellite products.

E. Evaluation of the Satellite Products

The ground observations were upscaled to the $5 \text{ km} \times 5 \text{ km}$ study area to validate the satellite products of Himawari-8 and MODIS. The all-sky DSR is taken into account despite the uncertainties in estimating the residual \bar{R} on cloudy days. Fig. 14 shows the temporal variation of the upscaled and satellite-derived DSR over a month. In general, the MODIS product shows better consistency with the upscaled DSR. Obvious overestimations can be found around the midday, especially under the clear-sky conditions since November 12. The reason can be partially attributed to the ignorance of topographic effects as the product matches better with the observed DSR on the flat hilltop. In fact, the method used in the MODIS product assumes that the aerosol optical depths for the “clearest” observation are known and its surface reflectance can be determined under Lambertian assumption [46]. The method treats the negative surface reflectance of the blue band as an observation containing cloud shadows. However, the topographic sheltering can be another possibility. Ignoring topographic effects may lead to large uncertainties on DSR estimation. Moreover, occasional underestimations occur on cloud-free and cloudy days throughout the month, which display less regularity and can be explained by random errors. The daily variation of the Himawari-8 DSR matches well with the upscaled DSR since November 7, though detailed fluctuations caused by clouds are smoothed by the 1-h temporal scale. But concentrating on the cloud-free days from October 30 to November 6, abnormal underestimations expose the considerable uncertainties of Himawari-8 products. Referring to the meteorological data measured by all-sky cameras, the land surfaces were covered by snows on the clear days. But the study area was marked as cloudy by the cloud-screening product of Himawari-8, which conforms with our previous study indicating the overestimation in cloud products of Himawari-8 [58]. It proves that the mistaken detection of clouds and snows may decrease the accuracy of DSR. Moreover, the parameterization method used in the Himawari-8 DSR product assumes that the effects of clouds and clear atmosphere can be decoupled. The planetary atmosphere is modeled as a clear sky atmosphere positioned above a cloud layer [45]. Although the method is simple to operate, the uncertainties should not be ignored. As the method is derived from the estimation of photo-synthetically available radiation (PAR) at the ocean surface, the topographic effects are also ignored, which further decreases the product’s accuracy over rugged terrains.

Scatter plots of the remotely sensed products and the upscaled observations on cloud-free days and cloudy days are presented in Fig. 15. The MODIS DSR product shows the best consistency with the upscaled DSR on cloud-free days. The R^2 , ME, and RMSE are 0.977, -0.459 W/m^2 , and 41.254 W/m^2 , respectively. On cloudy days, the errors grow larger and the scatter points become more dispersed around the regression line. It indicates that the uncertainties in DSR retrieval are strengthened by clouds. Under both conditions, the MODIS product exhibits a slight underestimation, which requires further evidence by adding more validation data in

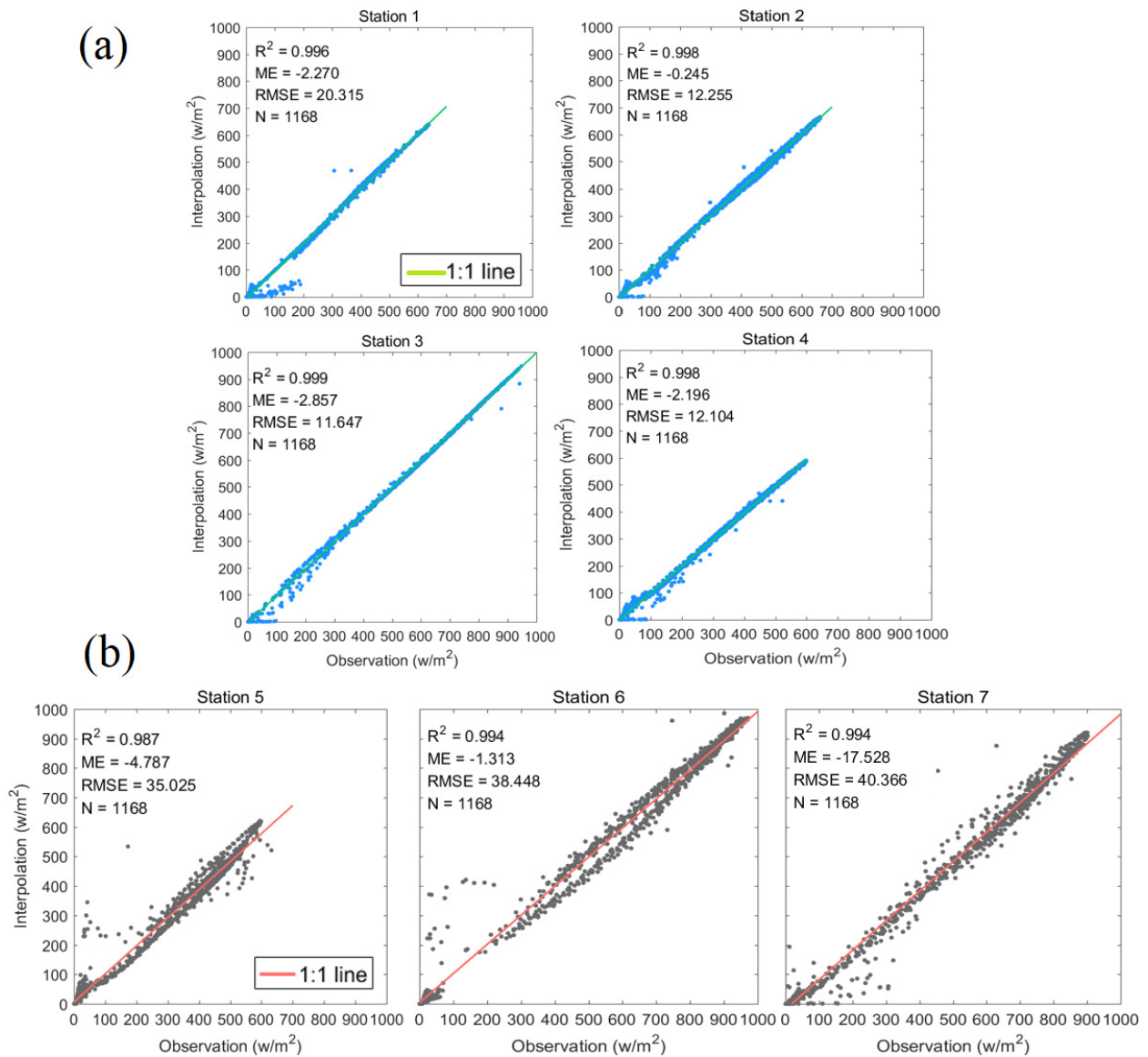


Fig. 12. Validation of the interpolated DSR on cloud-free days during a month. (a) Consistency between the estimated DSR and the observations at Stations 1–4 used for retrieving coefficients. (b) Consistency between the interpolated DSR and the observations at Stations 5–7 used for evaluating the interpolated accuracy.

the future. The Himawari-8 DSR product shows obvious errors on both cloud-free days and cloudy days, with RMSE around 60 W/m². It is uncommon that the errors on cloud-free days are larger than those on cloudy days. The mean errors over a month are -17.083 and -7.858 W/m², respectively. Such a phenomenon may be attributed to the mistaken detection of snows as clouds on clear days. On the whole, the two satellite DSR products are reliable at most time. The accuracy of the MODIS DSR data is higher than that of the Himawari-8 DSR. The uncertainties of them are considerable, underscoring the importance of better estimations on atmospheric conditions and topographic effects.

IV. DISCUSSION

A. Cloud Effects

Although the upscaled DSR on cloudy days was applied to validate the satellite products, the feasibility of the validation

method is obscure under such conditions. On cloudy days, the DSR pattern reflects the regional average values dominated by topography configurations, but the fluctuations caused by cloud effects are not ignorable at different ground stations. In theory, more ground stations contribute to the estimation of fluctuations and thus increase the accuracy of the residual \bar{R} . In practice, the insufficient samplings undermine the outcome of the Ordinary Kriging method. Still, Fig. 16(a) is presented to reflect cloud effects on DSR with the existing resources. Compared with DSR on cloud-free days, the contribution of residuals is more significant on cloudy days. With the increasing intensity of fluctuations, the residuals become larger indicating the enlarging differences between DSR pattern and the pixel-scale true values. Since the true values are inaccessible, the interpolated DSR at point-scale is validated at different temporal scales. As demonstrated in Fig. 16(b), with the lowering of temporal resolutions, the average error is reduced and the distributions of errors become more clustered.

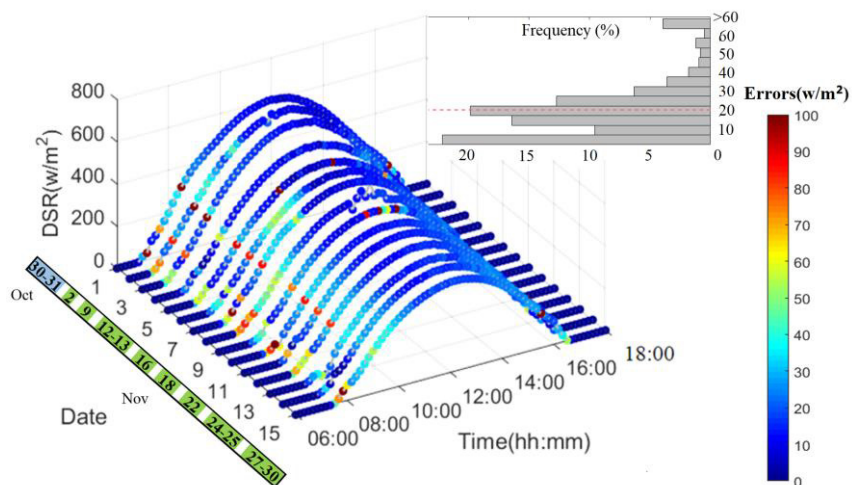


Fig. 13. Pixel-scale DSR on cloud-free days during a month. The labels on *x*-axis correspond to the orders of dates on the time axis. The *y*-axis represents the daytime, while the *z*-axis represents the pixel-scale DSR calculated by the interpolated and upscaling method. The markers' color indicates the validation errors of interpolated DSR, whose distribution is demonstrated by the histogram at the upper-right corner.

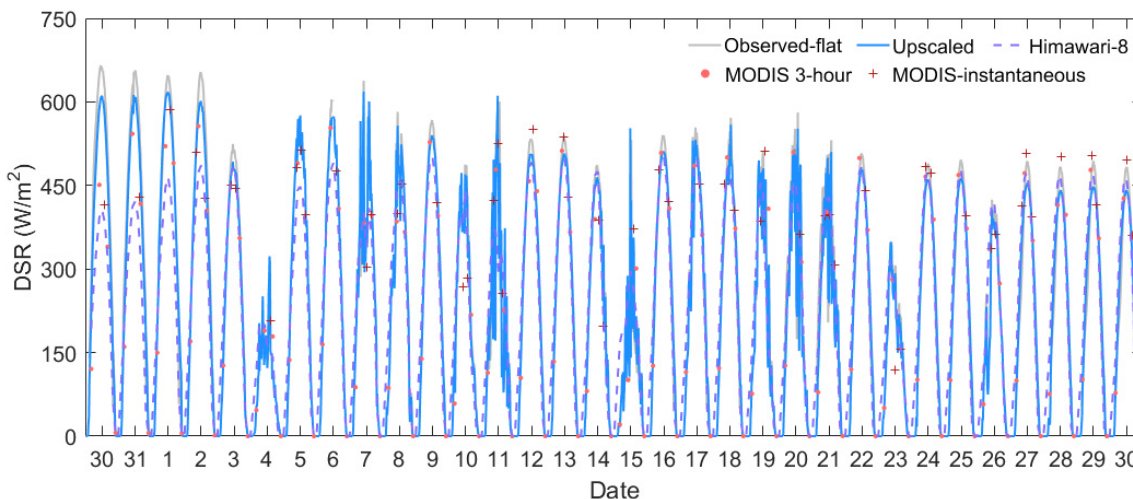


Fig. 14. Validations of the satellite DSR products on all-sky conditions. The gray solid line represents the observed DSR on the flat hilltop. The blue solid line indicates the upscaled DSR over the 5 km × 5 km study area. The red point and the brown cross indicate the 3-hourly interpolated and the instantaneous DSR provided by MODIS. The dashed purple line indicates the 1-h DSR provided by Himawari-8. The validation results are performed from October 30 to November 30, 2018.

In terms of instantaneous DSR, the average error remains equivalent to that in Fig. 13, though considerable errors take up a larger proportion. It proves that the interpolation method can be extended to all-sky conditions and the DSR pattern succeeds in representing the deterministic spatial average over a pixel-scale region. As a tradeoff between resolution and accuracy, 3-h averaged DSR is recommended as an ideal data set for the validation of satellite products under all-sky conditions. We hope that such a conclusion could offer far-reaching insight to the future production of standard data sets aiming at radiation validations over rugged terrains.

B. Comparison With the Stratified Sampling

Stratified sampling method has been widely adopted in spatial sampling procedures, which can also be applied to

locate ground stations and upscale point-scale measurements to pixel-scale. Claiming to have the potential in optimal capture of the variability within a region [59], [60], the stratified sampling strategy is selected as a comparison with our method. Prior to sampling, the study area was subdivided by auxiliary terrain parameters including slope, aspect, and *Vd*, which have the most significant influence on DSR over rugged terrains. Fig. 17(a) demonstrates an example of seven strata classified by the K-means method. Ground stations were chosen randomly within each stratum. The pixel-scale DSR is the sum of each *in situ* data weighted by the proportion of its representative zone. The DSR data sets simulated by LESS were treated as relative true values to evaluate the stratified sampling method. As shown in Fig. 17(b), the RMSE indicates upscaling errors over a cloud-free day. With the increase of

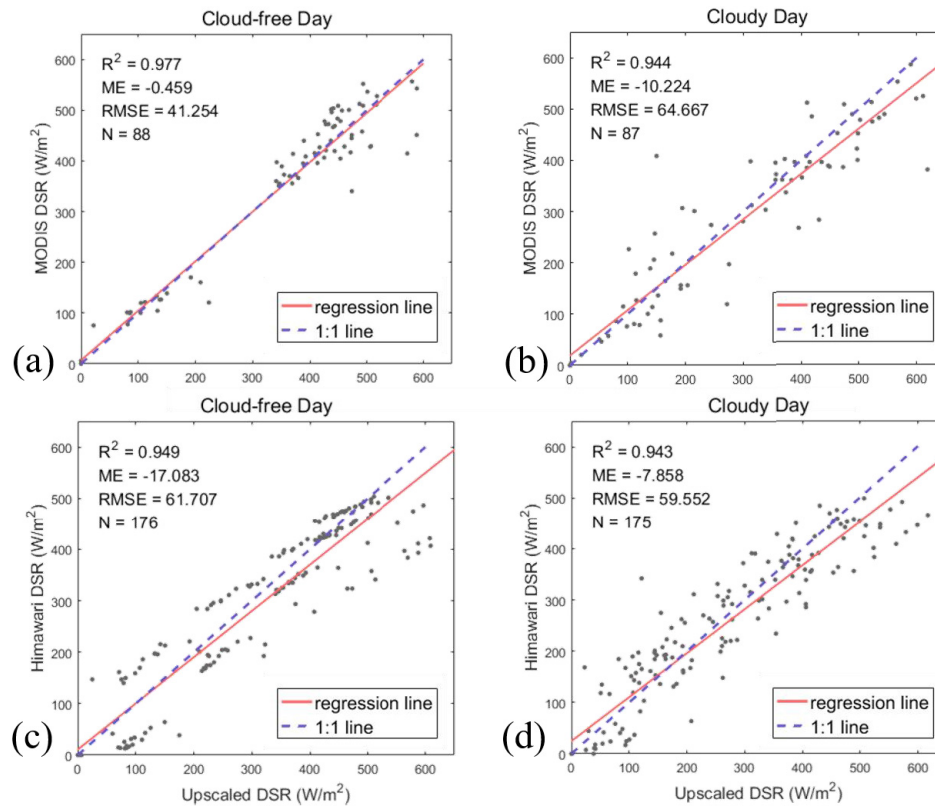


Fig. 15. Validations of the satellite DSR products on cloud-free days and cloudy days. (a) and (b) Comparison between the MODIS DSR and the upscaled DSR. (c) and (d) Comparison between the Himawari-8 DSR and the upscaled DSR. The red solid line is the regression line of the scatter points. The purple dashed line is the 1:1 line.

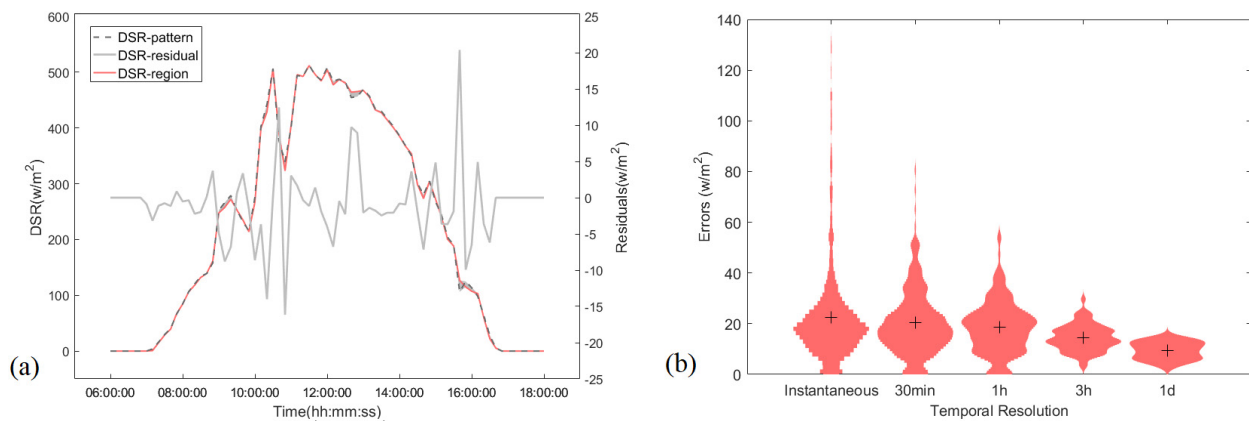


Fig. 16. Upscaled DSR and validation results of the interpolated DSR on cloudy days. (a) DSR pattern, pixel-scale DSR (corresponding to the left vertical axis), and the residuals (corresponding to the right vertical axis) over a cloudy day. (b) Cloud effects on the interpolated accuracy changing with temporal resolutions. The colored regions represent distributions of interpolated errors over a month, with the cross markers as average errors. Every colored region (histogram) is normalized individually so that the distribution shapes can be compared among different temporal scales.

station numbers (strata), the error line shows a decreasing trend with variant speed. The RMSE values are susceptible to the number of stations from 3 to 6, indicating large errors caused by insufficient sampling. When the station number exceeds 17, the RMSE levels off to stable values as enough samplings are collected. The stratified sampling method is more dependent on station numbers and shows inferior accuracy than that of our method, which indicates that four ground stations are sufficient to achieve the acceptable accuracy level. In other

words, the proposed interpolation and upscaling method have a great advantage over the traditional geostatistical algorithms in estimating pixel-scale DSR over rugged terrains.

C. Limitations and Further Study

It is undeniable that several limitations exist in our study. One of them is to use the Ordinary Kriging method in the prediction of residuals when sufficient samplings are

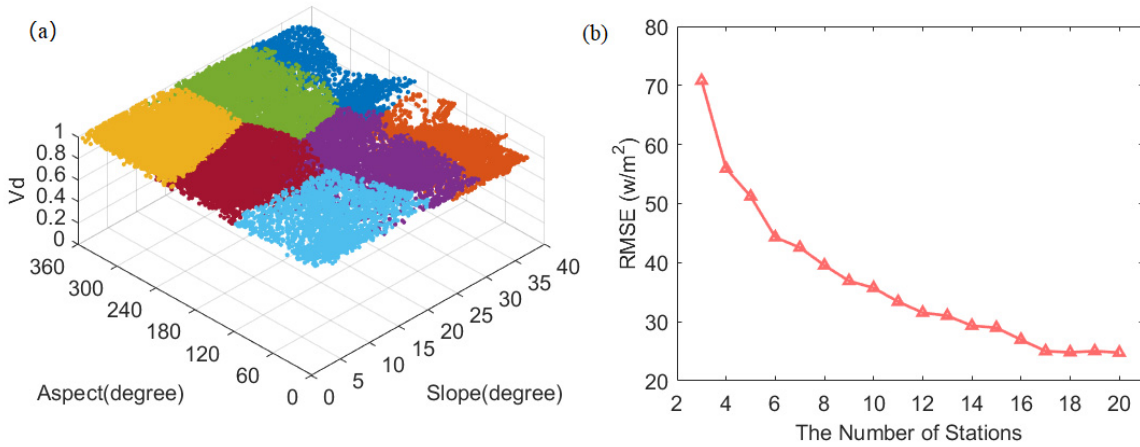


Fig. 17. Upscale DSR using stratified sampling method. (a) Strata divided by terrain factors. (b) Effects of the number of ground stations on upscaling errors.

TABLE II
INFORMATION OF THE GROUND STATIONS

Station	Longitude(°)	Latitude(°)	Altitude(°)	Slope(°)	Aspect(°)	Land cover
1	117.399	42.397	1848.551	9	85	Grass, roads nearby
2	117.398	42.397	1848.427	19	269	Grass
3	117.397	42.393	1852.700	26	196	Grass
4	117.395	42.393	1810.066	22	285	Grass, trees nearby
5	117.392	42.394	1700.166	2	47	Grass
6	117.390	42.396	1756.811	29	189	Grass
7	117.400	42.387	1838.169	30	138	Grass

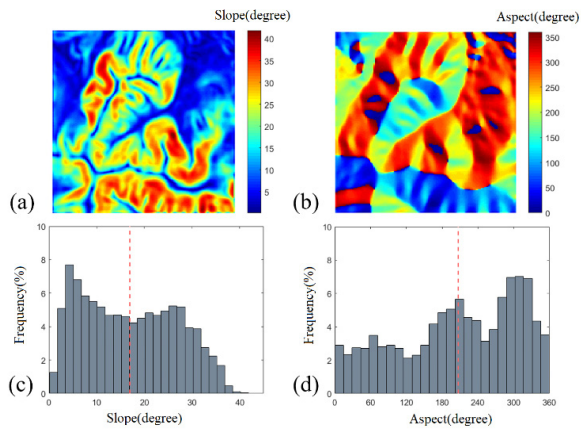


Fig. 18. Terrain parameters. (a) Spatial distribution of slope. (b) Spatial distribution of aspect. (c) Histogram of slope values. (d) Histogram of aspect values. Red dashed lines: averages of slope and aspect values.

inaccessible under constrained experimental resources. On cloud-free days, the problem seems inconsequential as the proportion and spatial variation of the residuals are insignificant. While on cloudy days, the residuals correspond with the radiation fluctuations caused by clouds, which show strong spatial heterogeneity. The most effective approach for enhancing the accuracy is to incorporate more observations at different slopes. The accompanied question is the locations of these stations, which require further study to take the

distribution of clouds into consideration. The parameters pertaining to cloud characteristics will be created and introduced to the current validation methodology. Another potential limitation stems from the reliability of upscaled DSR, which proves to be optimal and unbiased in theory but is unlikely to be examined by direct validation. As a compromise, additional observations at three ground stations were applied to evaluate the interpolated DSR in our study. More observations demand to be collected at different slopes to improve our confidence in the interpolated and upscaled results. The accumulation of long-time series observations will further ameliorate the reliability of pixel-scale validation results. In general, we will continue our experiments to compensate for the lack of data and to probe into further study on cloud effects.

V. CONCLUSION

Estimation of DSR is of great importance in global energy budget and climatic modeling. Rugged terrains have a strong influence on the energy, making the traditional flat-surface assumption unreasonable for estimating high-resolution DSR in mountainous areas. Although many topographic radiation models have been built up and corresponding satellite products have been issued for years, effective validation methods are absent for rugged terrains. It can be attributed to the lack of reliable field observed data, standard experiment procedures, and mismatch of spatial scales between point-scale observations and satellite products. Therefore, we

propose a computer-simulation-based validation methodology accompanied by a guideline for radiation measurements over rugged terrains.

Prior to the interpolation and upscaling of DSR, a radiative transfer model, LESS, was utilized as a tool for providing large-scale DSR as the reference truth. A point-to-point validation was performed to guarantee its reliability. We carried out field experiments to obtain point-scale observations. In the procedure of radiation measurements, the planes of radiometers were set exactly parallel to the underlying slopes. High-resolution DEM data and pre-defined spectral parameters served as essential inputs for the LESS model. The results showed that though the abrupt change of radiation was hard to be captured around sunrise and sunset time, the modeled and observed DSR exhibit good consistency at most time. The LESS satisfied our needs for pixel-scale DSR estimation.

Based on the verified LESS, we proposed a spatial interpolation and upscaling method of DSR over rugged terrains. A semi-empirical model was created to interpolate DSR by assimilating key terrain parameters, which is the core of our method. Based on the reference truth values from LESS, the ideal number and locations of ground station were chosen by Monte Carlo method. The coefficients for the semi-empirical model were obtained from the various ground observation we elaborately located. The Ordinary Kriging algorithm was applied to extend the model's feasibility by considering the variation of atmospheric conditions over a region. The validation results revealed that the average error for interpolated DSR was around 20 W/m^2 under all-sky conditions and 10 W/m^2 for upscaled DSR in theory. Although considerable errors occurred around sunrise and sunset time, coarse temporal resolutions could cover up the instantaneous discrepancies. As a trade-off between resolution and accuracy, 3-h averaged DSR was recommended as an ideal data set for the validation of satellite products at kilometer-scale pixel. The MODIS and Himawari-8 DSR products were chosen to be validated, whose accuracies were acceptable at the most time with correlation coefficients exceeding 0.94. But the uncertainties were considerably arisen from the inaccurate estimations of atmospheric conditions and the ignorance of topographic effects. Comparing with the traditional geostatistical methods, we only need a small number of ground stations to interpolate and upscale DSR with ideal accuracy. Such an advantage is crucial to DSR validation over rugged terrains, where the natural conditions deteriorate the difficulties of field experiments.

In general, this article answers some of the essential questions in the field validation over rugged terrains. It sheds light on how to interpolate and upscale ground-based observations to match the spatial scale of a remote sensing pixel. Since we can no longer ignore topographic effects on satellite products, we hope that our research can provide instructional suggestions for reasonable DSR validation at kilometer-scale over rugged terrains.

APPENDIX

Key terrain parameters were retrieved from the DEM data. Fig. 18 gives an example of the slope and aspect distributions over the $2 \text{ km} \times 2 \text{ km}$ study area in Fig. 1(a). The spatial

distribution of them demonstrates that the area is characterized by strong heterogeneity of topography, which fulfills our research objectives. The histograms further reveal that typical terrains can be found within the area, with slopes varying from gentle to steep and aspects covering every orientation. Other terrain parameters, such as the Boolean shadow factor Θ in (2) and the sky view factor Vd in (3), were calculated with ray-tracing algorithms in our study. For shadow factor, each pixel is treated as the start of a ray which is in the solar direction. The elevations of the pixels on the ray are recorded and if the ray does not pass the center of those pixels, interpolation of adjacent pixels' elevation will be necessary. With the recorded elevation and the horizontal distance between the targeted pixel and other pixels on the ray, elevation angles can be calculated. If the values of each elevation angle are smaller than solar elevation angle, the targeted pixel will not be shadowed by surrounding pixels. Otherwise, the binary coefficient will be set to 0. For sky view factor, the largest elevation angle between the targeted pixel and surrounding mountains is searched in 16 directions. With the distance between target and surrounding slopes increasing, more slopes will be omitted, and thus we add compensatory factors to weight these 16 directions. As the calculation of interpolation and trigonometric functions is more efficient compared with traditional algorithms equally concerning for every direction, this method is applied to our study.

The ground observations in Fig. 2 were measured at different stations, whose information is provided in Table II. The CNR4 net radiometers (Kipp&Zonen), consisting of a pyranometer pair and a pyrgeometer pair, were used to measure DSR whose wavelength ranges from 300 to 2800 nm. Before the experiment, all the radiometers were calibrated with a MR-60 net radiometer (EKO) to guarantee the consistency of measurements. The observed data sets were processed with rigorous quality control. We abandoned the abnormal data which resulted from instrumental problems such as low electricity and deviated observed planes caused by winds. The radiation curves which look smooth and consecutive are assumed to be the clear days' observations. Furthermore, the pictures taken by all-sky camera are used to check any possible cloud.

ACKNOWLEDGMENT

The authors would like to thank the group members who participated in the field experiments but are not on the author's list. They would like to thank the shortwave radiation data produced from Himawari-8 supplied by the P-Tree System, Japan Aerospace Exploration Agency (JAXA). They would also like to thank the production of MODIS downward shortwave radiation data (MCD18A1) by Dongdong Wang's research team.

REFERENCES

- [1] M. I. Budyko, "The effect of solar radiation variations on the climate of the Earth," *Tellus*, vol. 21, no. 5, pp. 611–619, Oct. 1969.
- [2] M. Wild, "Global dimming and brightening: A review," *J. Geophys. Res.*, vol. 114, 2009, Art. no. D00D16, doi: [10.1029/2008JD011470](https://doi.org/10.1029/2008JD011470).

- [3] M. Wild, D. Folini, C. Schär, N. Loeb, E. G. Dutton, and G. König-Langlo, "The global energy balance from a surface perspective," *Climate Dyn.*, vol. 40, nos. 11–12, pp. 3107–3134, Jun. 2013.
- [4] V. Ramanathan, "Aerosols, climate, and the hydrological cycle," *Science*, vol. 294, no. 5549, pp. 2119–2124, Dec. 2001.
- [5] Y. Ma *et al.*, "Estimation of the regional evaporative fraction over the Tibetan Plateau area by using Landsat-7 ETM data and the field observations," *J. Meteorolog. Soc. Jpn.*, vol. 85A, pp. 295–309, 2007.
- [6] H. Gilgen and A. Ohmura, "The global energy balance archive," *Bull. Amer. Meteorolog. Soc.*, vol. 80, no. 5, pp. 831–850, May 1999.
- [7] M. Wild, A. Ohmura, C. Schär, G. Müller, D. Folini, and M. Schwarz, "The global energy balance archive (GEBa) version 2017: A database for worldwide measured surface energy fluxes," *Earth Syst. Sci. Data*, vol. 9, no. 2, pp. 601–613, 2017.
- [8] A. Ohmura *et al.*, "Baseline surface radiation network (BSRN/WCRP): New precision radiometry for climate research," *Bull. Amer. Meteorolog. Soc.*, vol. 79, no. 10, pp. 2115–2136, Oct. 1998.
- [9] G. König-Langlo, R. Sieger, H. Schmithüsen, A. Bücker, F. Richter, and E. Dutton, *The Baseline Surface Radiation Network and its World Radiation Monitoring Centre at the Alfred Wegener Institute*. Geneva, Switzerland: World Meteorological Organization, 2013.
- [10] J. A. Augustine, J. J. DeLuisi, and C. N. Long, "SURFRAD—A national surface radiation budget network for atmospheric research," *Bull. Amer. Meteorolog. Soc.*, vol. 81, no. 10, pp. 2341–2357, Oct. 2000.
- [11] J. A. Augustine, G. B. Hodges, C. R. Cornwall, J. J. Michalsky, and C. I. Medina, "An update on SURFRAD—The GCOS surface radiation budget network for the continental United States," *J. Atmos. Ocean. Technol.*, vol. 22, no. 10, pp. 1460–1472, Oct. 2005.
- [12] D. Baldocchi *et al.*, "FLUXNET: A new tool to study the temporal and spatial variability of ecosystem-scale carbon dioxide, water vapor, and energy flux densities," *Bull. Amer. Meteorolog. Soc.*, vol. 82, no. 11, pp. 2415–2434, Nov. 2001.
- [13] C. Marty, R. Philipona, C. Fröhlich, and A. Ohmura, "Altitude dependence of surface radiation fluxes and cloud forcing in the alps: Results from the alpine surface radiation budget network," *Theor. Appl. Climatol.*, vol. 72, nos. 3–4, pp. 137–155, Sep. 2002.
- [14] M. Olefs *et al.*, "The austrian radiation monitoring network ARAD—best practice and added value," *Atmos. Meas. Techn.*, vol. 9, no. 4, pp. 1513–1531, 2016.
- [15] Y. Zhang, X. Li, and Y. Bai, "An integrated approach to estimate shortwave solar radiation on clear-sky days in rugged terrain using MODIS atmospheric products," *Sol. Energy*, vol. 113, pp. 347–357, Mar. 2015.
- [16] X. Li *et al.*, "Watershed allied telemetry experimental research," *J. Geophys. Res.*, vol. 114, 2009, Art. no. D22103, doi: [10.1029/2008JD011590](https://doi.org/10.1029/2008JD011590).
- [17] G. López, F. J. Batlles, and F. Rossi, "Deriving solar radiation in a mountain area from MODIS information," *Energy Procedia*, vol. 57, pp. 1092–1099, Jan. 2014.
- [18] C. Aguilar, J. Herrero, and M. J. Polo, "Topographic effects on solar radiation distribution in mountainous watersheds and their influence on reference evapotranspiration estimates at watershed scale," *Hydrol. Earth Syst. Sci.*, vol. 14, no. 12, pp. 2479–2494, 2010.
- [19] T. A. Schroeder, R. Hember, N. C. Coops, and S. Liang, "Validation of solar radiation surfaces from MODIS and reanalysis data over topographically complex terrain," *J. Appl. Meteorol. Climatol.*, vol. 48, no. 12, pp. 2441–2458, Dec. 2009.
- [20] P. Serrano-Ortiz *et al.*, "Surface-parallel sensor orientation for assessing energy balance components on mountain slopes," *Boundary-Layer Meteorol.*, vol. 158, no. 3, pp. 489–499, Mar. 2016.
- [21] B. Mayer, S. W. Hoch, and C. D. Whiteman, "Validating the MYSTIC three-dimensional radiative transfer model with observations from the complex topography of Arizona's meteor crater," *Atmos. Chem. Phys.*, vol. 10, no. 18, pp. 8685–8696, 2010.
- [22] S. Wu *et al.*, "Characterization of remote sensing albedo over sloped surfaces based on DART simulations and *in situ* observations," *J. Geophys. Res.*, vol. 123, no. 16, pp. 8599–8622, Aug. 2018.
- [23] J. Wen *et al.*, "Characterizing land surface anisotropic reflectance over rugged terrain: A review of concepts and recent developments," *Remote Sens.*, vol. 10, no. 3, p. 370, 2018.
- [24] P. M. Amatya, Y. Ma, C. Han, B. Wang, and L. P. Devkota, "Estimation of net radiation flux distribution on the Southern slopes of the Central Himalayas using MODIS data," *Atmos. Res.*, vol. 154, pp. 146–154, Mar. 2015.
- [25] M. Schwarz, D. Folini, M. Z. Hakuba, and M. Wild, "Spatial representativeness of surface-measured variations of downward solar radiation: Spatiotemporal representativeness of SSR," *J. Geophys. Res., Atmos.*, vol. 122, no. 24, pp. 13319–13337, Dec. 2017.
- [26] R. Dubayah and P. M. Rich, "Topographic solar radiation models for GIS," *Int. J. Geographical Inf. Syst.*, vol. 9, no. 4, pp. 405–419, Jul. 1995.
- [27] T. Wang, G. Yan, X. Mu, Z. Jiao, L. Chen, and Q. Chu, "Toward operational shortwave radiation modeling and retrieval over rugged terrain," *Remote Sens. Environ.*, vol. 205, pp. 419–433, Feb. 2018.
- [28] M. Z. Hakuba, D. Folini, A. Sanchez-Lorenzo, and M. Wild, "Spatial representativeness of ground-based solar radiation measurements—extension to the full meteor satellite disk," *J. Geophys. Res., Atmos.*, vol. 119, no. 20, pp. 11760–11771, Oct. 2014.
- [29] J. Tovar, F. J. Olmo, and L. Alados-Arboledas, "Local-scale variability of solar radiation in a mountainous region," *J. Appl. Meteorol.*, vol. 34, no. 10, pp. 2316–2322, Oct. 1995.
- [30] A. Sanchez-Lorenzo, M. Wild, and J. Trentmann, "Validation and stability assessment of the monthly mean CM SAF surface solar radiation dataset over Europe against a homogenized surface dataset (1983–2005)," *Remote Sens. Environ.*, vol. 134, no. 5, pp. 355–366, 2013.
- [31] G. Huang *et al.*, "Preliminary validation of GLASS-DSSR products using surface measurements collected in arid and semi-arid regions of China," *Int. J. Digit. Earth*, vol. 6, no. 1, pp. 50–68, Dec. 2013.
- [32] Y. Wei, X. Zhang, N. Hou, W. Zhang, K. Jia, and Y. Yao, "Estimation of surface downward shortwave radiation over China from AVHRR data based on four machine learning methods," *Sol. Energy*, vol. 177, pp. 32–46, Jan. 2019.
- [33] D. Hao *et al.*, "Estimating hourly land surface downward shortwave and photosynthetically active radiation from DSCOVR/EPIC observations," *Remote Sens. Environ.*, vol. 232, Oct. 2019, Art. no. 111320.
- [34] X. Li, "Characterization, controlling, and reduction of uncertainties in the modeling and observation of land-surface systems," *Sci. China Earth Sci.*, vol. 57, no. 1, pp. 80–87, Jan. 2014.
- [35] G. Huang, X. Li, C. Huang, S. Liu, Y. Ma, and H. Chen, "Representativeness errors of point-scale ground-based solar radiation measurements in the validation of remote sensing products," *Remote Sens. Environ.*, vol. 181, pp. 198–206, Aug. 2016.
- [36] B. Martínez, F. J. García-Haro, and F. Camacho-de Coca, "Derivation of high-resolution leaf area index maps in support of validation activities: Application to the cropland barrax site," *Agricult. Forest Meteorol.*, vol. 149, no. 1, pp. 130–145, Jan. 2009.
- [37] N. Cressie, "Statistics for spatial data," *Terra Nova*, vol. 4, no. 5, pp. 613–617, 1992.
- [38] R. Zhang, J. Tian, Z. Li, H. Su, S. Chen, and X. Tang, "Principles and methods for the validation of quantitative remote sensing products," *Sci. China Earth Sci.*, vol. 53, no. 5, pp. 741–751, May 2010.
- [39] J. Wang, Y. Ge, G. Heuvelink, and C. Zhou, "Upscaling *in situ* soil moisture observations to pixel averages with spatio-temporal geostatistics," *Remote Sens.*, vol. 7, no. 9, pp. 11372–11388, 2015.
- [40] S. Liu *et al.*, "Upscaling evapotranspiration measurements from multi-site to the satellite pixel scale over heterogeneous land surfaces," *Agricult. Forest Meteorol.*, vols. 230–231, pp. 97–113, Dec. 2016.
- [41] Y. Ge, Y. Liang, J. Wang, Q. Zhao, and S. Liu, "Upscaling sensible heat fluxes with area-to-area regression kriging," *IEEE Geosci. Remote Sens. Lett.*, vol. 12, no. 3, pp. 656–660, Mar. 2015.
- [42] G. Yin *et al.*, "A cost-constrained sampling strategy in support of LAI product validation in mountainous areas," *Remote Sens.*, vol. 8, no. 9, p. 704, 2016.
- [43] G. Yin, A. Li, and A. Verger, "Spatiotemporally representative and cost-efficient sampling design for validation activities in Wanglang experimental site," *Remote Sens.*, vol. 9, no. 12, p. 1217, 2017.
- [44] G. Yan *et al.*, "Temporal extrapolation of daily downward shortwave radiation over cloud-free rugged terrains—Part 1: Analysis of topographic effects," *IEEE Trans. Geosci. Remote Sens.*, vol. 56, no. 11, pp. 6375–6394, Nov. 2018.
- [45] R. Frouin and H. Murakami, "Estimating photosynthetically available radiation at the ocean surface from ADEOS-II global imager data," *J. Oceanogr.*, vol. 63, no. 3, pp. 493–503, Jun. 2007.
- [46] S. Liang, T. Zheng, R. Liu, H. Fang, S.-C. Tsay, and S. Running, "Estimation of incident photosynthetically active radiation from moderate resolution imaging spectrometer data," *J. Geophys. Res.*, vol. 111, 2006, Art. no. D15208, doi: [10.1029/2005JD006730](https://doi.org/10.1029/2005JD006730).
- [47] J. Qi *et al.*, "LESS: Large-scale remote sensing data and image simulation framework over heterogeneous 3D scenes," *Remote Sens. Environ.*, vol. 221, pp. 695–706, Feb. 2019.

- [48] J. Qi, D. Xie, D. Guo, and G. Yan, "A large-scale emulation system for realistic three-dimensional (3-D) forest simulation," *IEEE J. Sel. Topics Appl. Earth Observ. Remote Sens.*, vol. 10, no. 11, pp. 4834–4843, Nov. 2017.
- [49] J. G. Corripio, "Vectorial algebra algorithms for calculating terrain parameters from DEMs and solar radiation modelling in mountainous terrain," *Int. J. Geograph. Inf. Sci.*, vol. 17, no. 1, pp. 1–23, Jan. 2003.
- [50] S. Sandmeier and K. I. Itten, "A physically-based model to correct atmospheric and illumination effects in optical satellite data of rugged terrain," *IEEE Trans. Geosci. Remote Sens.*, vol. 35, no. 3, pp. 708–717, May 1997.
- [51] J. Dozier and J. Frew, "Rapid calculation of terrain parameters for radiation modeling from digital elevation data," *IEEE Trans. Geosci. Remote Sens.*, vol. 28, no. 5, pp. 963–969, Sep. 1990.
- [52] H. Alt and M. Godau, "Computing the Fréchet distance between two polygonal curves," *Int. J. Comput. Geometry Appl.*, vol. 5, no. 1, pp. 75–91, Mar. 1995.
- [53] T. Eiter, and H. Mannila, "Computing discrete Fréchet distance," Ph.D. dissertation, Dept. Inf. Syst., Tech. Univ. Vienna, Vienna, Austria, 1994.
- [54] Q. Y. Duan, V. K. Gupta, and S. Sorooshian, "Shuffled complex evolution approach for effective and efficient global minimization," *J. Optim. Theory Appl.*, vol. 76, no. 3, pp. 501–521, Mar. 1993.
- [55] N. Cressie, "Spatial prediction and ordinary Kriging," *Math. Geol.*, vol. 20, no. 4, pp. 405–421, May 1988.
- [56] J. A. Ruiz-Arias, T. Cebeauer, J. Tovar-Pescador, and M. Šúri, "Spatial disaggregation of satellite-derived irradiance using a high-resolution digital elevation model," *Sol. Energy*, vol. 84, no. 9, pp. 1644–1657, Sep. 2010.
- [57] Z. Li, M. C. Cribb, F.-L. Chang, A. Trishchenko, and Y. Luo, "Natural variability and sampling errors in solar radiation measurements for model validation over the atmospheric radiation measurement southern great plains region," *J. Geophys. Res.*, vol. 110, 2005, Art. no. D15S19, doi: 10.1029/2004JD005028.
- [58] Q. Chu, Y. Liu, and G. Yan, "A cloud detection algorithm for Tiangong-2 remote sensing data over the tibetan plateau," in *Proc. Tiangong-2 Remote Sens. Appl. Conf.*, 2018, pp. 82–93.
- [59] J.-F. Wang, G. Christakos, and M.-G. Hu, "Modeling spatial means of surfaces with stratified nonhomogeneity," *IEEE Trans. Geosci. Remote Sens.*, vol. 47, no. 12, pp. 4167–4174, Dec. 2009.
- [60] A. Grafström and L. Schelin, "How to select representative samples," *Scandin. J. Statist.*, vol. 41, no. 2, pp. 277–290, Jun. 2014.



Guangjian Yan (Senior Member, IEEE) received the Ph.D. degree from the Institute of Remote Sensing Applications, Chinese Academy of Sciences, Beijing, China, in 1999.

He is currently a Professor with the State Key Laboratory of Remote Sensing Science, Faculty of Geographical Science, Beijing Normal University, Beijing. His main research interests are multiangular remote sensing, vegetation remote sensing, and radiation budget.



Qing Chu received the B.S. degree in applied meteorology from China Agricultural University, Beijing, China, in 2014. She is currently pursuing the Ph.D. degree with Beijing Normal University, Beijing.

She was also a Ph.D. Student with the Institute for Atmospheric and Climate Science, ETH Zurich, Zurich, Switzerland, from 2017 to 2019. Her research interests include topographic radiation modeling in all-sky and radiation observation in mountainous areas.



Yiyi Tong received the B.S. degree in physical geography from Beijing Normal University, Beijing, China, in 2017, where she is pursuing the master's degree.

Her research interests include the estimation of radiation budget, validation of remote sensing models over rugged terrains, and vegetation modeling.



Xihan Mu received the B.S. degree in computer science and technology from the College of Information Science and Technology, Beijing Normal University, Beijing, China, in 1999, and the Ph.D. degree in remote sensing from the School of Geography, Beijing Normal University, in 2009.

He was a Visiting Student with the Laboratoire des Sciences de l'Images, de l'Informatique et de la Télédétection, Louis Pasteur University, Strasbourg, France, in 2007, and a Visiting Scientist with the Commonwealth Scientific and Industrial Research Organization (CSIRO) in 2016. He is with the State Key Laboratory of Remote Sensing Science, Institute of Remote Sensing Science and Engineering, Faculty of Geographical Science, Beijing Normal University. His research interests focus on multiangular remote sensing, particularly in the retrieval/measurement of vegetation structural parameters.



Jianbo Qi received the Ph.D. degree from Beijing Normal University, Beijing, China, in 2019.

He was a joint-Ph.D. Student with Paul Sabatier University, Toulouse, France, from 2016 to 2018. He is an Assistant Professor with Beijing Forestry University, Beijing. His research interests include 3-D radiative transfer modeling, realistic forest scene simulation, and vegetation parameter retrieval.



Yingji Zhou received the B.S. degree in mapping and geography information system from Beijing Normal University, Beijing, China, in 2015, where he is currently pursuing the master's degree in science.

His research interests include the estimation of downward shortwave radiation under all-sky conditions and time scale extend in high latitude areas. He has devoted his efforts to the application of deep learning technology in remote sensing.



Yanan Liu received the B.S. degree in mathematics and applied mathematics from the China University of Geosciences, Beijing, China, in 2015. She is pursuing the Ph.D. degree with Beijing Normal University, Beijing.

Her research interests include the neural network and the estimation of solar radiation on cloudy sky. She has also devoted her efforts to the data fusion of polar orbit satellite and geostationary satellite.



Tianxing Wang received the Ph.D. degree in GIS/Remote sensing from Beijing Normal University, Beijing, China, in 2011.

He is an Associate Professor with the School of Geospatial Engineering and Science, Sun Yat-sen University, Guangdong, China. He has authored or coauthored more than 90 scientific articles. His research interests focus on derivation of land surface biophysical parameters from satellite data, land surface radiation budget over rugged terrain for all-sky conditions, atmospheric CO₂ monitoring, multi- and hyper-spectral data processing, and remote sensing applications.



Kai Yan received the B.S. degree in mapping and surveying from the Beijing University of Civil Engineering and Architecture, Beijing, China, in 2011, and the Ph.D. degree in GIS/RS from Beijing Normal University, Beijing, in 2018.

He was a Visiting Scholar with the Department of Earth and Environment, Boston University, Boston, MA, USA, from 2014 to 2016. He is with the School of Land Science and Techniques, China University of Geosciences, Beijing. He was involved in the generation and assessment of official MODIS/VIIRS global leaf area index (LAI) and fraction of photosynthetically active radiation absorbed by vegetation (FPAR) products. His research interests include the bidirectional reflectance distribution function (BRDF) modeling and LAI/FPAR retrieval.



Donghui Xie received the Ph.D. degree in remote sensing and geographic information systems from Beijing Normal University, Beijing, China, in 2005, where she is currently an Associate Professor with the State Key Laboratory of Remote Sensing Science, Institute of Remote Sensing Science and Engineering, Faculty of Geographical Science.

Her research interests include canopy radiative transfer modeling, biophysical parameter retrieval of vegetation and remote sensing data fusion.



Shengbo Chen received the Ph.D. degree from the College of Geoexploration Science and Technology, Jilin University, Changchun, China, in 2000.

He is a Full Professor with the College of Geoexploration Science and Technology, Jilin University. His research interests include application of remote sensing in geology, agriculture, and exploration of the lunar system.



Wuming Zhang received the Ph.D. degree from Tsinghua University, Beijing, China, in 2004.

He is a Professor with the State Key Laboratory of Remote Sensing Science, Institute of Remote Sensing Science and Engineering, Faculty of Geographical Science, Beijing Normal University, Beijing.

His main research interests are photogrammetry and remote sensing, especially LiDAR point cloud processing and applications.



Hongmin Zhou (Member, IEEE) received the Ph.D. degree in remote sensing and geographic information systems from Beijing Normal University, Beijing, China, in 2018.

She is a Senior Engineer with the State Key Laboratory of Remote Sensing Science, Faculty of Geographical Sciences, Beijing Normal University/Chinese Academy of Sciences, Beijing.

Her research interests include land surface radiation budget, land surface parameters retrieval from various remotely sensed data and land surface products validation.